1 # Towards real-time seismic monitoring of a geothermal
2 # plant using Distributed Acoustic Sensing.

3 **Authors**: Jérôme Azzola[1], Katja Thiemann[2], Emmanuel Gaucher [1]
4 [1]Karlsruhe Institute of Technology (KIT), Institute of Applied Geosciences (AGW), Karlsruhe,
5 Germany
6 [2]Stadtwerke München GmbH, Munich, Germany.
7
8 **Corresponding author**: Jérôme Azzola (jerome.azzola@kit.edu)

10 # Abstract

11 Distributed Acoustic Sensing (DAS) is an emerging technology for acquiring seismic data on virtual
12 sensors densely distributed along an optical fiber. The broadband response of the sensors, associated
13 with the possibility of deploying fiber optic cables in harsh conditions and the relatively moderate cost
14 of this sensing element gives clear perspectives for DAS in geothermal wells to contribute to the
15 monitoring operations of geothermal plants. However, the technical feasibility of managing the large
16 flow of data generated by the DAS and the suitability of the strain-rate acquisitions to monitor locally
17 induced seismicity is yet to be assessed.

18 We propose a monitoring concept establishing DAS as an effective component of the seismic
19 monitoring of the Schäftlarnstraße geothermal plant (Munich, Germany). The underlying data
20 management system links the existing on-site infrastructure, including the fiber optic cable deployed
21 in one of the site's injection wells and the associated DAS recorder, to a cloud Internet-of-Things (IoT)
22 platform designed to deliver both a secure storage environment for the DAS acquisitions and
23 optimized computing resources for their processing. The proposed solution was tested over a period
24 of six months and showed the feasibility of efficiently acquiring and processing the large flow of
25 continuous DAS data. For seismic risk mitigation purposes, we additionally investigate the potential of
26 the monitoring concept to tend towards real-time monitoring. The processing outcomes, focusing
27 especially on two detected local seismic events, demonstrates the relevance of DAS from geothermal
28 wells for the (micro)seismic monitoring of the geothermal site. Despite the noisy operational
29 conditions, the applied processing workflow takes advantage of the sensors' high spatial density for
30 data denoising and event triggering and highlights that higher detection sensitivity than conventional
31 seismometers can be achieved. From a different perspective, further analyses of the DAS records
32 confirm the logging capabilities of the technology, especially regarding well completion integrity.

33 The 6-months test period shows that permanent DAS can be integrated as a routine seismic
34 monitoring component of geothermal plants and advantageously complement surface seismometer-
35 based networks, especially in urban environments.
36

1. Introduction

37

38 Geothermal energy has been exploited with considerable success in the Greater Munich area
39 (Germany) since the late 1990s (Agemar et al., 2014; Dussel et al., 2016). The geological conditions in
40 southern Bavaria are particularly suitable for extracting heat from the geothermal fluid of the Upper
41 Jurassic layers of the Molasse basin (Schulz and Jobmann, 1989; Agemar et al., 2012). A growing
42 number of energy companies located in the north and the south of Munich benefit from the
43 geothermal resource to supply the district heating network with renewable energy, making it an
44 important driver of the ecological revolution of the region (e.g. Farquharson et al. (2016)). As part of
45 this effort, SWM GmbH, the energy provider of the Munich city, wants to cover the district heating
46 demand with CO2-neutral resources by 2040 at the latest, predominantly from geothermal energy
47 (Cröniger et al., 2022).

48 The development of the geothermal energy branch in the Munich region has resulted in a significant
49 increase in knowledge, in particular about the geological setting of the region (Böhm et al., 2013).
50 However, the spread of deep geothermal energy exploitation still entails its challenges. Producing heat
51 and electricity from geothermal fluids leads to changes in the stress-state prevailing in the subsurface.
52 Recent observations and analyses showed that these perturbations can possibly induce seismicity,
53 even in hydrothermal systems driven by a porous matrix (Kraft et al., 2009;
54 Megies and Wassermann, 2014; Seithel et al., 2019). Therefore, seismic monitoring outcome is a key
55 aspect in the operation of deep geothermal reservoirs. With the on-going developments in the Munich
56 region, the extension of the existing monitoring networks and the development of innovative
57 monitoring strategies are important elements for seismic risk mitigation. Their full integration into the
58 plant operation could benefit to a more secure and sustainable management of the geothermal
59 resource, especially if the seismic monitoring results can feed numerical models aiming at forecasting
60 the thermo-hydro-mechanical response of the geothermal system to operational conditions
61 (e.g. Gaucher et al. (2015); Grigoli et al. (2017)).

62 Distributed Optical Fiber Sensors (DOFS, see e.g. Hartog (2017) for an extensive review on the
63 technology) offer attractive perspectives to support the geothermal plant operation in a variety of
64 contexts. The operating principle behind fiber optic sensing is based on the use of an optoelectronic
65 system delivering spatially resolved measurements along the optical fiber to which it is connected.
66 Scattering effects occurring along the optic fiber make it possible to acquire various physical
67 parameters on virtual sensors distributed along the length of the fiber, such as changes in dynamic
68 strain (Distributed Acoustic Sensing, DAS), changes in static strain (Distributed Strain Sensing, DSS) and
69 changes in temperature (Distributed Temperature Sensing, DTS). Hence, these technologies open up
70 new opportunities in terms of logging, imaging and monitoring. DAS, which is the focus of this article,
71 has developed, in the last decades, as an emerging geophysics instrument and has been applied in
72 seismic analysis with established quality performance (see e.g. Parker et al. (2014);
73 Lindsey et al. (2020) or Paitz et al. (2021)). In the field of borehole seismic acquisitions, applications
74 are as varied as production control, integrity supervision, or seismic monitoring
75 (see Johannessen et al. (2012); Parker et al. (2014); Li et al. (2015) for reviews on possible
76 applications). DAS technology gained early acceptance in the oil and gas industry (Baldwin, 2014) and
77 demonstrated great potential as a long and dense seismic antenna, for instance in vertical seismic
78 profiling (VSP) applications (Madsen et al., 2012; Mateeva et al., 2012; Harris et al., 2016; Miller et al.,
79 2016). The potential for time-lapse monitoring of reservoirs was also demonstrated, e.g. by
80 Mateeva et al. (2014). The imaging capabilities of the distributed measurement also benefit the
81 identification of flows and production zones. Naldrett et al. (2018) show that DAS data can be used
82 for the analysis of fluid-entry points and gain further quantitative information about the production
83 zones. In terms of seismic monitoring, the technology has shown great success in capturing signals as

84   varied as microseismic (Lellouch et al., 2020) or teleseismic events (Ajo-Franklin et al., 2019) in a
85   variety of contexts and settings.

86   In the geothermal energy community, the potential of the technology stems in particular from its
87   versatility and ability to acquire, along boreholes, different parameters relevant for the monitoring of
88   the geothermal system. Hence, several fiber types in one single FOC can deliver DTS, DSS and DAS
89   measurements. Depending on the deployment design, which remains challenging for deep (hot)
90   boreholes, this can provide information on temperature profiles, well completion integrity, in- and
91   out-flow zones of the geothermal fluid, induced seismicity, etc. (Koelman, 2011; Koelman et al., 2012;
92   Van Der Horst et al., 2013). For seismic monitoring, DAS along the borehole allows sensors to be
93   positioned much closer to the reservoir than surface seismometers, thus closer to the potential
94   seismicity. The high spatial sampling achieved with DAS along the optical fiber also gives another
95   perspective to the seismic monitoring, by considerably densifying the set of observations.
96   Consequently, borehole DAS may significantly contribute to the seismic monitoring, as long as the FOC
97   is properly coupled to the ground and the well is not a permanent source of noise.

98   In order to assess the DAS (and DTS) technology, two wells of the newly developed geothermal plant
99   at Schäftlarnstraße (SLS), south of Munich (Germany), have been equipped with FOCs (see Fig.1a). At
100   the SLS site, the amount of DAS data to be collected with this equipment goes up to several tens of
101   megabytes per second. The collection and processing of this data flow can be a serious challenge,
102   particularly when secure and fast remote access to the data is required to integrate the monitoring
103   results into the operation of the geothermal plant. Hence, appropriate data management and
104   processing infrastructures are necessary for the DAS system to become a real-time continuous
105   component of the geothermal system monitoring. In this paper, we demonstrate the technical
106   feasibility of implementing a DAS-based continuous and permanent seismic monitoring in an
107   operational environment - the SLS site. The present study is a unique case to our knowledge and
108   constitutes a proof of concept for future implementations. The proposed concept aims at managing
109   the different phases of the monitoring, from the acquisition to the archiving and the processing of the
110   DAS data. It has been developed to efficiently meet the requirements in terms of data transfer rate,
111   amount of data, level of access to data and scalability. With regards to the data processing, screening
112   for possible local induced seismicity was implemented, allowing us to assess the capabilities of the
113   system in terms of seismic event detection. The opportunity to test the concept was given during a
114   six-month continuous acquisition period, from February to July 2022.

115   The first part of the manuscript presents the infrastructure that was implemented on the SLS site to
116   integrate the data storage and processing modules into a cloud based IoT platform, and which
117   interconnects the DAS recorder and Azure, the cloud application platform distributed by Microsoft.
118   Then, we focus on the data processing and detection workflows developed on the cloud-based
119   platform, providing insights into the recording conditions and the denoising strategies applied to
120   enhance the signal of interest and achieve a satisfactory level of detection. The highlights of the 6-
121   months trial period are presented in the third part of the manuscript, focussing on two local
122   microseismic events that have been efficiently detected by the proposed monitoring system. Finally,
123   the results of the trial period are discussed. We first concentrate on the utilization of DAS in the routine
124   operation of the geothermal plant, considering the logging and monitoring capabilities demonstrated
125   at the SLS site. Then, we elaborate on the potential of the proposed concept for real-time seismic
126   monitoring of geothermal power plants. We conclude by discussing how the monitoring concept can
127   contribute to the development of a reservoir management system aiming at continuously guiding the
128   operator in exploiting the geothermal resource in an efficient and sustainable manner.
129

130
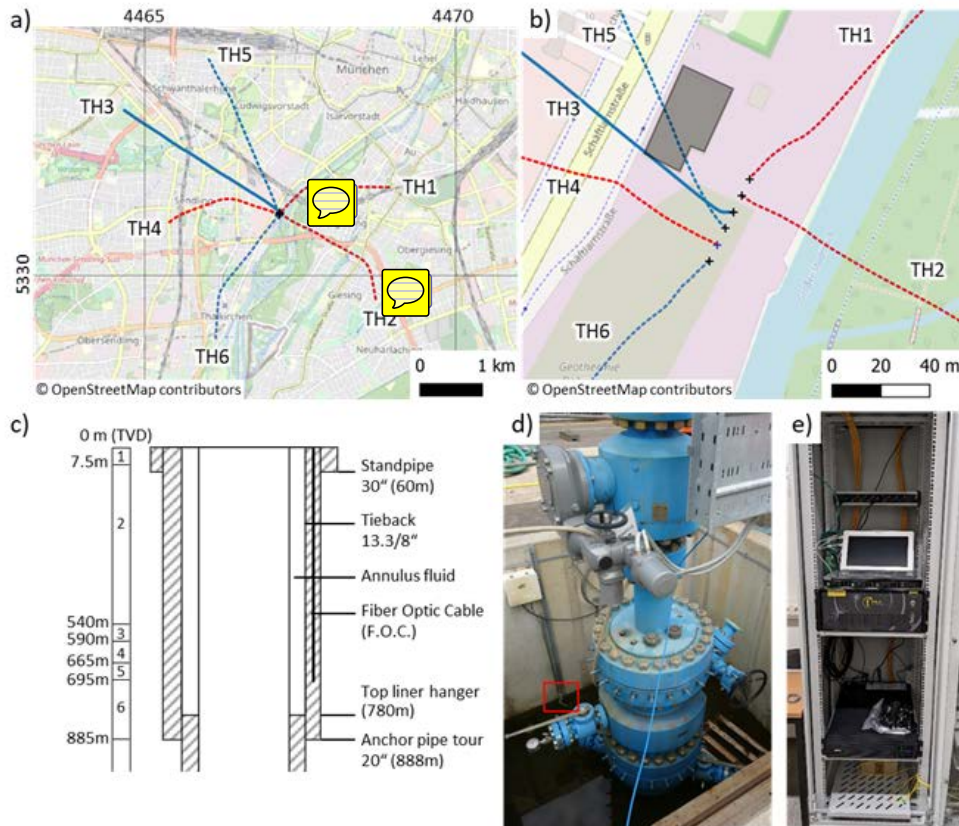
Figure 1: Overview of the study site. Panel a): location of the geothermal power plant in the southern part of Munich city and projection on the surface of the 6 well trajectories. Red lines denote production wells and blue lines show injection wells. The Gauss-Kruger 4 coordinate system is used for the Northing and Easting markers. Panel b): focus on the powerplant. The gray polygon shows the location of the control room in which the Febus A1-R interrogator and recording system has been installed on the well site. Panel c): structure of the well TH3 along its first 900 m. The FOC deployed from surface to 700 m (TVD). The installation allows the section to be probed repeatedly, the interrogated fiber forms a U-loop. The well is vertical in the section of interest. The column on the left shows the stratigraphy. Numbers 1 to 6 stand respectively for Quaternary, "Obere Süßwasser Molasse" (OSM), "Süßbrackwasser Molasse" (SBM), "Obere Meeresmolasse" (OMM) "Glaukonit Sande" (OMM), "Blättermergel" (OMM), "Neuhofener Schichten". Panel d): picture of TH3 wellhead. The red rectangle highlights the entry point of the FOC in the ground. Panel e): picture of the setup in the control room. It shows the DAS recorder, the Uninterrupted Power Supply (UPS) and the peripheral devices, which are all secured in a metallic enclosure.

145

2. The DAS monitoring system

2.1. On-site infrastructure and data acquisition

2.1.1. Schäftlarnstraße geothermal site

Geothermal energy plays an important role in making Munich the first major German city to produce 100 % of its district heating from renewable energy by 2040 (e.g. Farquharson et al. (2016); Cröniger et al. (2022)). As part of this ambition, Stadtwerke München GmbH (SWM) developed in the Munich city, at Schäftlarnstraße (SLS), one of the largest inner-city geothermal plants in order to cover the heating needs of 80.000 citizen. Hence, from the end of April 2018 to the end of May 2020, three geothermal doublets (i.e. six wells) were drilled and tested. All wells are deviated and reach the geothermal water-bearing rock layer of the Upper Jurassic period - the Malm - at about 2500 m below sea level (Schulz and Jobmann, 1989; Böhm et al., 2013). In Figure 1a, the trajectories of the production (red lines) and injection (blue lines) wells are projected on the map of the Munich city center. Figure 1b focuses on the well site. It highlights the proximity of the wellheads that are separated by about 8 m from each other. The wells start to significantly deviate from about 800 m below surface.

The technical concept of the geothermal site of Schäftlarnstraße, based on three doublets drilled from the same pad, contributes to raising the standards of deep geothermal energy exploitation in the region.

2.1.2. On-site FOC equipment

Monitoring is a key component for the operation of geothermal plants and the SLS project goes beyond the standards in this domain. Fiber optic cables have been deployed in the TH3 and TH4 wells (see Fig. 1) in order to benefit from DOFS and the possibility to turn optical fibers into a collection of sensors. A precise description of the cable settings and their implementation can be found in Schölderle et al. (2021).

The coupling of the FOC to the surrounding medium plays a crucial role in DAS technology applications. At the SLS geothermal field, two different configurations exist (Schölderle et al., 2021). The TH3 cable has been cemented behind the casing of the well, along the vertical section extending from surface to about 700 m (see Fig. 1). The TH4 cable is deployed inside the production well, from wellhead to total depth, using a sucker rod. Cemented cables do not interfere with well operations, and generally provide tighter mechanical coupling to the surrounding, which is favorable for the acquisition of high-quality DAS data (Reinsch et al., 2013). On the contrary, Martuganova et al. (2021) report on possible disturbing signals which may be observed with free-hanging cables in geothermal wells due to poor cable-to-well coupling. While the TH4 cable can be recovered and replaced, if necessary, this is not the case for the permanent TH3 cable, whose installation must be done carefully to avoid any damage during run-in-hole and to ensure well integrity with appropriate cementing job. In the present study, we use exclusively the FOC deployed in TH3, due to the unavailability of the TH4 cable at the time of the trial monitoring period.

Figure 1c focuses on the TH3 completion over the first 700 m along which the FOC was deployed. This section is considered as being vertical, since its average deviation angle calculated from the borehole trajectory is 3°. On one side, the cemented FOC faces the shallow geological layers: Quaternary, "Obere Süßwasser Molass" (OSM), "Süßbrackwasser Molasse" (SBM) and "Obere Meeresmolasse"

187 (OMM). On the well side, it faces an annulus filled with fluid, a tie-back. Beyond the tie-back flows the
188 reinjected geothermal fluid, which enters the Malm reservoir from the open-hole section of the well
189 (between 2571 m and 3049 m TVD).

190 In practice, the FOC in TH3 makes a U-loop at its end that provides redundant probing of the vertical
191 section from surface to 700 m. Figure 1d shows the entry and exit points of the FOC at the TH3
192 wellhead (red square). Finally, both ends of the cable are accessible in the control room next to the
193 well pad (gray polygon in Fig. 1b).

2.1.3. DAS set-up for the test period

195 For the 6-months monitoring period, a Febus Optics A1-R recording system has been connected to the
196 sensing fiber in the control room for continuous acquisition of DAS. The device is based on the phase-
197 coherent optical time domain reflectometry (OTDR) technique. The principle consists in measuring the
198 phase differences in the backscattered photons from neighbouring positions along the fiber. This
199 enables recording dynamic strain data, or strain-rate (SR), over short distances called gauge-lengths
200 (GL) and at several positions along the fiber (see Juškaitis et al. (1994) for an experimental validation
201 of the sensing technique). An extensive description of the possible DAS settings can be found in
202 Masoudi and Newson (2016) and in Hartog et al. (2013). Figure 1e shows the installation in the SLS
203 control room, where the recording system (or recorder) is connected to an uninterrupted power
204 supply (UPS). The UPS ensures the delivery of a stable alternating current to the equipment and
205 prevents short power interruptions. All devices are stored and secured in a metallic shelter.

206 Considering the location of the DAS recorder relative to the well pad, the DAS records contain the
207 signal acquired along the TH3 loop, but also the signal from the control room to the TH3 wellhead.
208 Hence, the portions of cable at surface and in the upper part of the well are particularly subject to
209 disturbances arising from human activity, such as circulation of heavy vehicles or operations on the
210 well pad. The same applies to the DAS recorder installed in the control room. In Section III, we further
211 discuss the impact of the recording conditions on the data.

212 The physical position of the virtual sensors distributed along the interrogated fiber has been identified
213 from a tap-test at the wellhead (Fig. 1d). This calibration procedure accounts for the acquisition
214 parameters, in particular the fixed 10 m GL applied to the acquisitions. The spatial sampling is further
215 improved using a 50 % spatial overlap of the GL and benefiting from the redundant probing that results
216 from the U-loop fiber. The analyzed DAS datasets feature thereby a 2.5 m spatial sampling, which
217 corresponds to a distribution of 280 virtual sensors along the first 700 m of TH3. In the time domain,
218 the sampling frequency is set at 500 Hz.

219 To ensure optimal signal quality, the velocity and frequency of the expected seismic waves should
220 guide the selection of the acquisition parameters. Among these specifications, the GL is of particular
221 importance and should minimize the so-called gauge length effect (e.g. Dean et al (2017)).
222 Insufficiently long gauge lengths degrade the signal to noise ratio, while, in case of excessive gauge
223 lengths, the resolution of the measurements is degraded, and the shape of the observed wavelet
224 distorted. The focus with the proposed DAS monitoring is on the detection of microseismic events
225 potentially induced at a local scale (i.e. in a radius of 5 km) during the operation of the plant, i.e. while
226 the geothermal fluid circulates between the wells within the reservoir. Hence, local seismicity is the
227 monitoring focus which oriented the selection of the DAS acquisition parameters. Considering the
228 surrounding environment of the fiber - apparent velocities from 1000 to 3000 m/s - and the targeted
229 frequency range - between 5 and 40 Hz - we applied a fixed GL of 10 m. Hence, the ratio of apparent
230 wavelength to GL is expected to provide a reliable assessment of the actual wavelength
231 (Dean et al., 2017), while the acquired datasets remain finely sampled in space.

2.2. Description of the cloud infrastructure

An inherent constraint of DAS is the possibly huge amount of data it generates. This is particularly impactful in the context of continuous and permanent DAS. Hence, to guarantee stable and reliable acquisition of the data by the DAS recorder, it is recommended to externalize the processing using appropriate computational resources. Ensuring secure remote access to the stored data is another constraint which has to be managed in order to integrate the DAS system into the geothermal plant monitoring. These specifications motivated the development of a dedicated data archiving and processing cloud platform. With the acquisition set-up characteristics described previously, 5.04 GB large binary files are generated hourly by the recorder in the form of individual Hierarchical Data Format 5 (HDF5) files. The DAS files are written on the solid-state drive (SSD) of the recorder, which behaves as a fast and efficient buffer. Besides, the Febus A1-R has been connected to the second component of the monitoring system, namely a cloud platform.
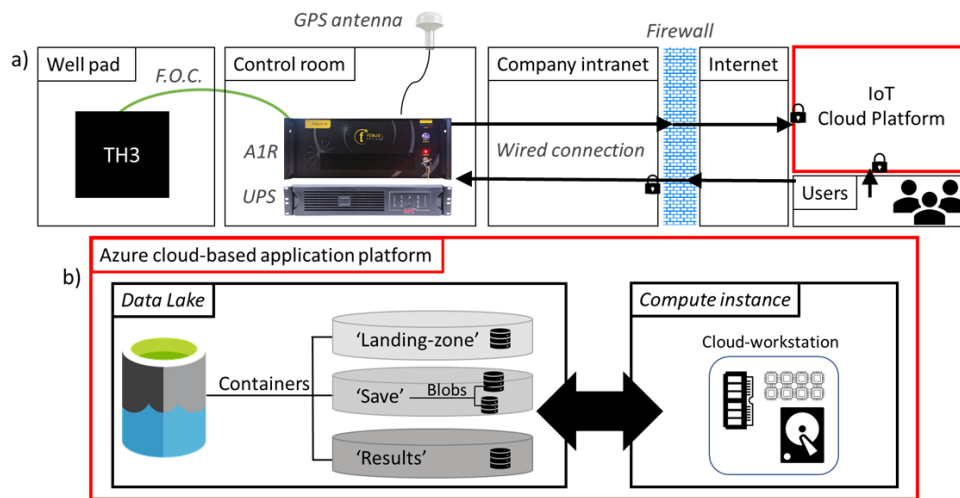
Figure 2: Panel a): schematic view of the monitoring system proposed to link the TH3 FOC, the Febus A1-R recorder, the developed IoT cloud platform and the users or developers of the infrastructure. Keys are meant to highlight a secured connection. Panel b): focus on the conceptual structure of the IoT cloud platform developed to connect the Febus A1-R recorder to Microsoft's cloud-based application platform, Azure. It is subdivided into two entities able to communicate through standardized data exchange. Azure Data Lake constitutes the data storage solution, which is organized into "Containers" and "Blobs". The associated structure is comparable to the more common directory and file system. Azure compute instances (or cloud workstations) are used to process the datasets using scalable resources.

2.2.1. The Azure cloud application platform

Figure 2a illustrates the monitoring and data management system. The system links the onsite infrastructure (i.e. well pad and control room devices) to the Internet of Things (IoT) cloud platform developed to host specific archiving and processing modules. The setup ensures an efficient and secure data flow via the company's intranet and enables a hierarchical remote connection of the users to both the recorder and the cloud platform.

261   The IoT cloud platform is described in more detail in Fig. 2b. It is based on *Azure*, Microsoft's cloud
262   application platform, which bundles a set of public IaaS (Infrastructure as a Service) and PaaS (Platform
263   as a Service) services. A detailed review of the available Azure services can be found in
264   Soh et al. (2020a, 2020b). Two interconnected applications, namely *Azure Data Lake Storage* and
265   *Azure ML Studio*, have been selected to fulfil the data archiving and processing tasks. These Azure
266   services meet the data management system's requirements in terms of amount of stored data, level
267   of access and efficiency of IT processing.

268   2.2.2. Data storage solution

269   The storage of the hourly generated DAS binary files is ensured by the big data solution called *Azure*
270   *Data Lake Storage* (left hand-side of Fig. 2b). The large and numerous files generated during the 6-
271   months continuous monitoring are saved on a so-called data lake. This storage environment offers a
272   scalable and hierarchical file system which is based on *Azure Blob*, a proprietary solution dedicated to
273   storing objects in the cloud. The latter is optimized for storing large amounts of unstructured data,
274   such as textual or binary data. In the following, the storage environment on the cloud-platform is
275   named data lake.

276   Figure 2b also focuses on the structure of the data lakes, whose management is assigned to an Azure
277   user account. The sketch distinguishes the three types of resources available to the user to organize a
278   set of stored items. The data lake can be subdivided in so-called containers, which include themselves
279   the blobs, i.e. the resources associated to individual data binary files generated by the recorder, or
280   results from the data processing. The three previously mentioned structures (i.e. account, containers
281   and blobs), can be respectively compared to file systems, folders and files, which are more familiar
282   objects in IT.

283   An important aspect of the storage system is the access right management. Secured and delegated
284   access to the resources is ensured by the use of Shared Access Signature (SAS) tokens. Every resource
285   is therefore assigned a unique address making it possible to grant user-customized permissions and
286   access rights. Another key feature of the chosen storage solution is the ability to manage the costs
287   associated with the storage requirements. It involves organizing the saved data according to the
288   frequency of access and the duration of storage, by assigning appropriate levels of access to the stored
289   objects. Typically, the blobs located in the "*Save*" container (see Fig.2b) are saved after processing and
290   are granted with an access level which is optimized for storing infrequently accessed data. This tier
291   provides lower storage costs but larger latency and delays in the data access. The same applies for the
292   blobs of the "*Result*" container, which archives the objects resulting from the processing flow. Hence,
293   the properties of the data storage environment allowed all the produced resources to be stored
294   seamlessly, including the entire 6-months long time series of DAS data. On the contrary, the blobs in
295   the "*Landing Zone*", i.e. the storage area containing files awaiting processing, are granted with tiers
296   that are designed to achieve high performances in reading and exchanging data.

297   2.2.3. Data processing solution

298   The computing instances constitute with the cloud-based workstations the computational resources
299   of the system (right side of Fig. 2b) and are available from the *Azure ML Studio*. This cloud based
300   solution allows developing, running and automating the launch of notebook-based scripts from an
301   online workspace.

302   A key aspect of these workstations is their adaptability, which enables the user to scale the available
303   resources according to its needs, in terms of supplied hardware (for example, number of physical and
304   logical cores) and accessible services (linkage to desired tools and libraries). The system illustrated in

305   Fig. 2a has been designed to process the DAS data entering the "*Landing Zone*" on an hourly basis.
306   Hence, the workstation has been scaled to sustain significant memory and CPU-to-memory loads, to
307   enable the large DAS files to be loaded in the workstation Random Access Memory (RAM).
308   Additionally, the workstation has been configured to use Python-based codes suitable for the seismic
309   record processing and the underlying Obspy library (Beyreuther et al., 2010).

310   The workstations also have the advantage of providing direct access to the computational resources
311   being queried. This feature avoids the queuing system typically associated with High Performance
312   Computing (HPC) clusters.

3. Data processing workflows

314   The cloud-based processing of the acquired DAS data aims at providing a catalogue of possible induced
315   seismicity with the associated waveforms. The Python scripts running on an hourly basis from the
316   cloud-based workstations are intended to read and structure the DAS files landing in the Data Lake in
317   the form of blobs and apply the seismological processing workflow.

3.1 Data structuring

319   The reading of the blobs of the "*Landing Zone*" is done from the computing instance using the
320   dedicated Python client package. Secure access to the blobs storing the DAS acquisitions is ensured
321   via the SAS-tokens assigned to the container. Once the strain-rate data of a given blob is loaded in the
322   cloud workstation RAM, it is structured as a 2D dataset of one hour duration, extending spatially from
323   the surface to a depth of 700 m TVD. Using the results of the tap-test carried out at the wellhead
324   (see Sect. 2.1), we extract the 280 traces localized along TH3 and assign a physical location, i.e. a
325   vertical depth, to each corresponding virtual sensor. The resulting 2D dataset, which has a spatial and
326   temporal sampling of 2.5 m and 2.0 ms respectively, enters the seismological processing workflow
327   (featuring data denoising and event detection) as an Obspy stream (Beyreuther et al., 2010).

3.2. Data denoising

329   Compared to conventional seismometers, seismic records obtained using DAS systems generally
330   exhibit higher noise levels and stronger interferences (e.g. Correa et al. (2017);
331   Olofsson and Martinez (2017)). The causes of these disturbances may be multiple and their impact on
332   the records can vary along the cable. Lindsey et al. (2020) review several factors influencing the quality
333   of the DAS data, from the recorder and sensor environment to the sensing method itself. DAS
334   recordings have therefore been subject to various developments in denoising methods, benefiting
335   notably from the high spatial sampling of the acquired data and the spatial coherence of the observed
336   wavefields.

337   While one dimensional time-frequency Butterworth filters are effective to suppress noise in a
338   frequency band of interest, the aforementioned characteristics of the DAS datasets allow the
339   application of various 2D denoising approaches inherited from array processing and active seismics.
340   Among those, spectral filtering in the frequency-wavenumber (*f-k*) domain
341   (Duncan and Beresford, 1994) can be applied to suppress the energy associated with identified
342   disturbances or incoherent noise, which may result in an enhancement of the signal-to-noise ratio
343   (Isken et al., 2022).

344
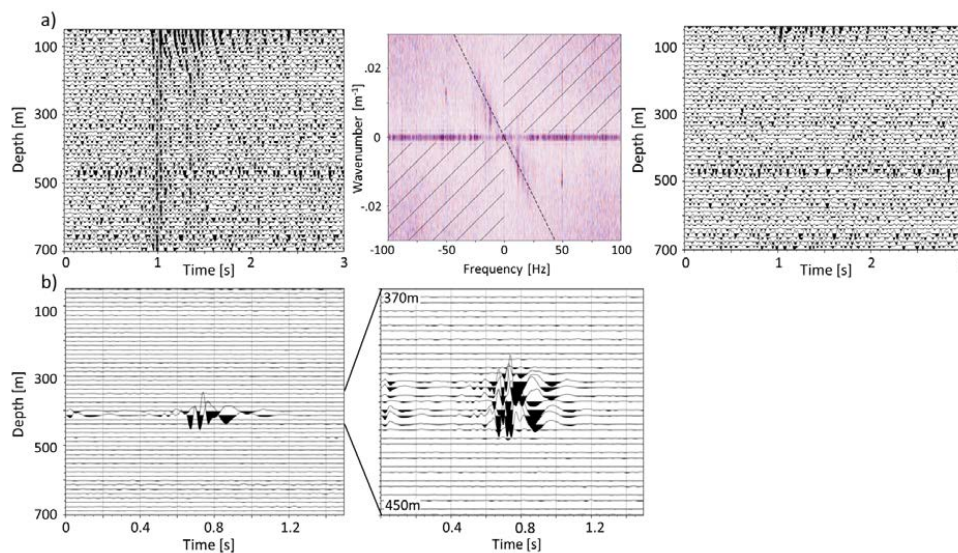
Figure 3: Overview of different types of noise recorded in the target frequency band. For visual and illustrative reasons, the dataset is first filtered below 100 Hz. Panel a) focusses on the impact of the surface activity associated with the industrial operating site at which the acquisitions are conducted. From left to right, the filtered dataset is shown in the depth-time domain, then in the frequency-wavenumber (f-k) domain and, finally, back into the depth-time domain once filtered in the f-k domain. The f-k filtering consists in keeping the shaded areas (middle figure) and suppressing the energy related to known noise sources. Panel b) shows an example of a strong local signal related to operational activities carried out in a nearby well, in the depth-time domain.

Here, the one-hour strain-rate datasets are bandpass filtered in the 5 to 40 Hz frequency band, which corresponds to a typical frequency range for the detection of local induced seismicity (e.g. Maurer et al. (2020)). However, as noted in the Sect. 2.1, the geothermal power-plant activity strongly impacts the acquisitions in the target frequency band. Figure 3a illustrates two types of anthropogenic disturbances typically recorded along the fiber. First, the DAS recorder may vibrate in its rack which leads to the recording of high amplitude signals which are overprinted on all dataset traces. Such spiky signals are attributed to laser-noise (Zhirnov et al., 2019) and can lead to spurious detections. Secondly, surface activity occurring close to the well may generate acoustic waves propagating in the fluid within the tie-back (see Fig. 1c). These acoustic waves may eventually be transmitted to the fiber, resulting in the observation of down-going waves propagating at a velocity of about 1500 m/s. Consequently, to avoid numerous false detections, the datasets are additionally filtered in the *f-k* domain. Our approach consists in keeping, in the *f-k* domain, the energy of the waves propagating from the lowest part of the fiber towards the surface. This is justified by the fact that potential local seismic events should originate from deeper than 700 m. The middle panel of Fig. 3a shows the above described dataset in the *f-k* domain, highlighting the propagation of the previously identified waves: the ones propagating along the entire fiber at an infinite velocity, visible on the horizontal axis in the *f-k* domain, and those propagating from the surface at velocities typical of acoustic waves in fluids, leading to high energy components in the positive wavenumber - negative frequency domain or vice-versa (i.e. top-left or bottom-right quarter). One can also observe, in the *f-k* domain, a strong 50 Hz component, which is typical of noise induced by the alternating current of the electrical grid. Hence, the filtering consists in isolating the positive wavenumber - positive

374 frequency domain or vice-versa (i.e. the shaded part of the *f-k* domain). As shown on the left part of
375 Fig. 3a, the proposed approach successfully removes the previously identified waves.

376 Additional strong noises, which impact the dataset locally, may not be filtered by the proposed
377 processing flow, as shown in Fig. 3b. The spiky signals isolated here were recorded during the lowering
378 of an electric submersible pump (ESP) in a nearby well. Hence, Fig. 3b illustrates how completion
379 operations can also influence the recordings, especially as the inter-well distances remain short at the
380 investigated depths. However, these types of local noise sources do not result in spurious detection,
381 considering the workflow proposed for the event detection.

3.3. Event detection

383 Once properly structured and filtered, the dataset of interest enters the detection workflow, which is
384 based on a recursive STA/LTA approach (Withers et al., 1998; Trnkoczy, 2012) implemented in the
385 Obspy library (Beyreuther et al., 2010). The chosen detection parameters are given in Table 1:

386 *Table 1: Event detection parameters based on a recursive STA/LTA and a coincidence sum.*

Trigger activation (STA/LTA ratio)	Trigger off (STA/LTA ratio)	Short-Time Average (STA)	Long-Time Average (LTA)	Coincidence sum
2.3	1.3	0.3 s	3 s	30

387 The detection workflow uses the multiple distributed traces of the DAS datasets and includes the
388 computation of a coincidence sum. This approach, which is commonly applied with large networks of
389 sensors, consists in combining all single station triggers to identify possible time overlaps that will be
390 interpreted as synchronous events. Hence, the coincidence sum gives the number of individual
391 overlapping triggers (Withers et al., 1998; Trnkoczy, 2012). In our application, a detection occurs when
392 the coincidence sum exceeds 30 traces (see Table 1). For neighbouring locations, this corresponds to
393 simultaneous triggering over about 70 m of fiber. Nevertheless, no constraint was provided regarding
394 the clustering of the single triggers over depth.

395 Once a 1-hour DAS dataset is processed, the detection report (i.e. list of triggers, including detection
396 time, triggered trace, etc.) is appended and saved in the "*Results*" container together with the
397 corresponding waveforms, i.e. six-seconds long data subsets centred on each detection and written in
398 miniseed format. On average, the full processing of a one-hour long DAS file (5.04 GB) takes
399 11 minutes with 8 processors (2,7 GHz Intel Xeon® Platinum 8168) on the cloud workstation.

400 The detection results are occasionally downloaded locally for quality control and post-processing,
401 which includes the picking of the seismic phases. The results of the post-processing of two
402 microseismic events are presented in Sect. 4.

4. Monitoring results

404 During the survey, 4122 files have been acquired, saved and processed following the described
405 procedure. Over the 6-months period, the DAS recorder recorded continuously except for short
406 periods during which the GPS signal was lost. This section presents the results obtained in terms of
407 detections and dataset characterisation.

4.1. Spectral content of the DAS records

As an initial evaluation of the collected DAS data, we analyze the frequency content using probabilistic power spectral densities (or PPSD, see e.g. McNamara (2004)). PPSD is commonly used to assess statistically the noise levels at different frequencies. To obtain noise levels representative of the day and night fluctuations, we analyze 48 hours of strain-rate data collected. At each sensor, the PPSD is computed from 192 data segments of 30 minutes. The median of each PPSD is calculated and a stack of all the resulting frequency profiles is presented in Fig. 4. The target frequency band of this analysis, 5 to 40 Hz, is delimited by dashed lines. The image shows a strong impact of anthropogenic activities at shallow depth, over the first 50 m, in this frequency domain.
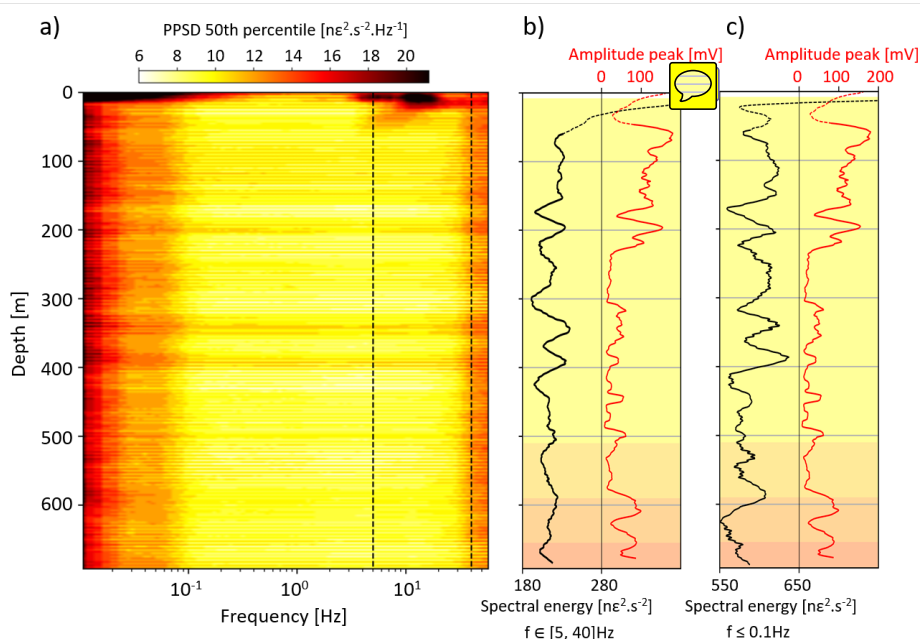
Figure 4: Spectral content of the DAS records at the study site. Panel a): Evolution with depth of the frequency content of strain-rate data acquired on two consecutive days. The probabilistic power spectral density (PPSD) is computed from each time-series, using 192 data segments of 30 minutes. The colour scale indicates the median PPSD at the sensor depth. The target frequency band, from 5 to 40 Hz, is bounded by the dashed lines. Panel b): Evolution with depth of the spectral energy (the integral of the PPSD) in the 5 - 40 Hz frequency range (black curve). Panel c): Same as panel b, but for the energy below 0.1 Hz (black curve). In panels b) and c), the amplitude of TH3 cement bond log (CBL) is shown over depth in red and the lithological changes are highlighted by the coloured background (see Fig. 1c) for the corresponding units). Note that the spectral energy curve and the CBL amplitude have been filtered with a moving average filter of 10 m.

This shallow influence is highlighted in the central part of the figure, which focuses on the evolution with depth of the spectral energy between 5 and 40 Hz (black curve). Below 100 m, the curve shows that the noise conditions do not significantly improve with depth anymore. The right part of the figure focuses on the lowest frequencies of the shown spectra, below 0.1 Hz. The variation in depth of the spectral energy has similar fluctuations in this low frequency range than in the target frequency band.

433 In both frequency bands, we highlight local fluctuations which affect the entire spectrum. The origin
434 of these noise sources can be multiple. A specific attention is given to the topic in Sect. 5.1, especially
435 with regard to the cement bond log (CBL) acquired in TH3 and shown in red in Fig. 4.

4.2. Local seismic event analysis

4.2.1. Seismic event detection

438 During the monitoring period, several regional and a couple of local seismic events have been
439 detected. To assess the capability of the DAS to monitor induced local seismicity, we focus in this
440 paragraph on the two detected local seismic events. The first one, of local magnitude M_L 1.5, occurred
441 on February 2022, the 9th and has been extensively recorded by the surface seismic stations operated
442 locally, in a radius of 10.4 km (see Azzola et al. (2021) or Azzola et al. (2022)). The second one occurred
443 on April 2022, the 22nd. Its characteristics have not been evaluated yet. Besides the DAS
444 measurements presented here, this second event was hardly identified by a three-component
445 seismometer deployed in a nearby well and was not observed from the surface network. This suggests
446 that the event has a magnitude lower than the completeness of the surface network magnitude, i.e.
447 Mw 0.7 (Azzola et al., 2021).

448 Figure 5 shows the bandpass- and *f-k* filtered strain-rate data associated with the February (panel a)
449 and April (panel b) events. The bandpass-filtered datasets are additionally shown in Appendix A (see
450 Fig. A1) to emphasize the effect of the denoising strategy in the *f-k* domain on the spatial coherence
451 of the strain-rate acquisitions. The left panels of Fig. 5 give an overview of the multiple arrivals that
452 can be identified in the DAS records. The middle and right panels focus on the first P- and the first S-
453 waves, respectively. Both wave types are clearly discriminated from their apparent velocities along
454 the fiber, which is larger for the P-wave than for the S-wave. Interestingly, one can also observe that
455 the S-wave maximal amplitude is larger than for the observed P-wave. The figure also highlights the
456 distinctive characteristics of both events. In Figure 5a), i.e. for the February event, successive scattered
457 P- and S-waves can be observed in the 3-second data-window, and the first S-wave is dominant at a
458 frequency of 8 Hz, lower than the P-wave frequency, around 25 Hz. The higher frequency content of
459 the April event captured in Fig. 5b), the lower delay between the P- and S- waves, and the lack of
460 multiple scattered waves are characteristics of a nearby event.

461 In addition, multiple phases with different polarizations, including the first P- and S-waves, have been
462 clearly recorded for both events (Fig. 5). This shows that the insensitivity of the TH3 fiber to
463 horizontally polarized waves is not a major constraint to properly identify onset times of local events.
464
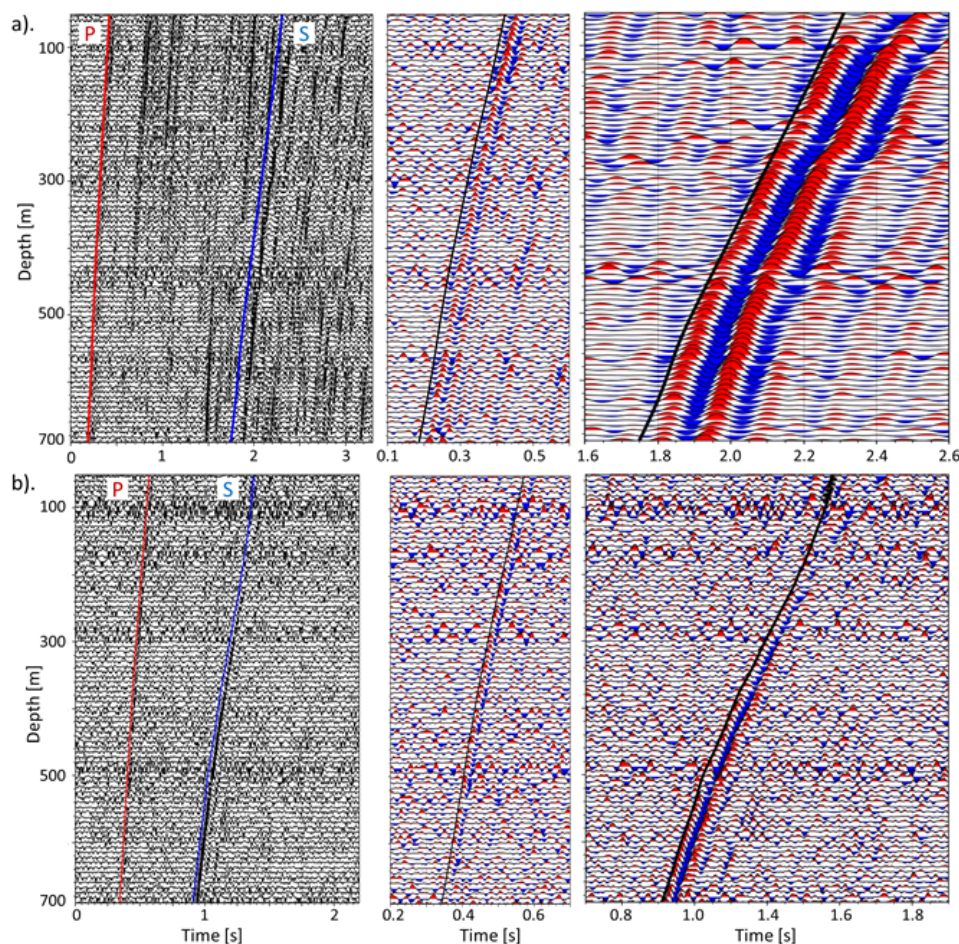
Figure 5: Strain-rate of the local February (panel a) and April (panel b) seismic events detected on the entire interrogated fiber. The left panels show the multiple arrivals including the first P- and S-waves. The middle and right panels focus on the first P- and first S-arrivals, respectively. The plain curves show the results of the semi-automatic first arrival picking approach. Panel a): the February event is located about 10 km away from the SLS geothermal site and has a magnitude of M_L 1.5. The horizontal axis indicates seconds after 2022.02.09 05:51:30.7 (UTC). Panel b): April event. The horizontal axis shows seconds after 2022.04.22 13:26:11.8 (UTC).

4.2.2. Onset-time picking

For both local events, we display in Fig. 5 the evolution with depth of the P- and S- waves arrival times (see continuous black curves). The onset times have been obtained using a semi-automated picking procedure applied – for the time-being – outside the cloud. The reason for the non-automation of the procedure is the necessary *ad-hoc* definition of a picking guide function supported by three user-defined picks. The procedure follows standards applied in active borehole or surface seismic processing. For each analyzed time-series, it consists in finding the break time (zero-crossing) in a search window defined around the guide function.

481 Figure 5 shows that the first P-wave arrivals have been consistently identified over the entire fiber for
482 both events. Nevertheless, although the automatic picking for the S-wave is correct along most of the
483 fiber, this is not true for the shallowest, nor the deepest part of the fiber. For the first 100 m
484 (respectively 200 m) associated with the April (February) event, the origin is likely the larger
485 background noise evidenced at these depths, which is not totally discarded by the applied filtering.
486 For the February event, the strongest, the interference between the S-wave and the multiple P-waves
487 comes in addition to the effect of the surface activity.

488 The automatic picking technique was applied trace by trace and was not exploiting the array
489 properties of the DAS, in particular the signal coherency recorded along the fiber. This characteristic,
490 which is well-known and used in VSP-processing, offers perspective to improve the seismic event
491 processing sequence.

4.2.3. Preliminary event and site characterization

493 A precise location and characterization of both local events from the DAS data will be the focus of
494 future work. However, for preliminary characterization, Wadati diagrams (Wadati and Oki, 1933) have
495 been computed using the most consistent part of the P- and S-arrival times. The corresponding Wadati
496 diagrams are presented in Appendix B (Fig. B1). Approaches based on Wadati diagrams have their
497 limitations, especially as the isotropy and homogeneity of the propagation medium may be an
498 irrelevant hypothesis depending on the location of the events with respect to the sensors. However,
499 the diagram can provide a first estimate of the April 22 origin time, which compensates for the lack of
500 additional seismic observations. Hence, the estimated origin time is 2022-04-22 13:26:11.77 (UTC).
501 When accounting for the period of the analyzed phases, an error of 0.02 s can be attributed to the
502 estimate. Furthermore, the vertical antenna formed by the DAS allows partial localization of the event,
503 using the travel distances computed along the fiber from the aforementioned origin time. Considering
504 an average P-wave velocity of 3000 m/s leads to an origin at a depth of 1700 m TVD (1180 m under
505 mean sea level) with a horizontal offset of 500 m from the DAS antenna. Hence, this April event likely
506 has its origin in the Tertiary sedimentary cover, rather than in the geothermal reservoir (Malm-Jurassic
507 formation).

508 The Wadati diagram is also used to analyze changes in the apparent P- to S-wave velocity ratio (VP/VS)
509 along the fiber. The diagram highlights two distinct trends, with an inflection point at approximately
510 500 m, at the end of the so-called "Obere Süßwasser Molass" formation (OSM). The observed
511 apparent VP/VS ratios are of 2.5 and 2.2 respectively for the superficial and the deeper parts.

512 For both events, the vertical profile of the P- and S-wave arrival times can also be used to characterize
513 the variations along the FOC of the apparent velocity of the identified seismic phases. The result is
514 illustrated in Fig. 6. Each apparent velocity profile is computed by differentiating the associated arrival
515 time profile and by applying a moving average filter of 100 m and 130 m for the P- and S-waves
516 respectively. The profiles obtained for both events are consistent in terms of spatial location of the
517 local minima and maxima, for both P- and S-waves. These apparent velocity variations may be
518 positioned along the lithological column, as displayed in the figure as different shades of yellow. All
519 profiles highlight strong variations, notably inside the thick OSM formation, which is mainly composed
520 of clay marl, sand and gravel layers. The apparent velocity changes observed may indicate variations
521 of the geomechanical properties, and outline the layered structure of the formation, at a local scale.

522 In terms of absolute amplitudes, the profiles calculated for the S-waves show a difference of 200 m/s
523 at their maximum, which is reached at the interface between the layers "3" and "4". However, the
524 absolute velocity estimates observed for both events should be compared carefully, considering that
525 Fig. 6 focusses on apparent velocities measured along the vertical FOC. The February event originates
526 from the Malm reservoir several kilometres away from TH3 while the April event occurred much closer

and shallower. Considering the location of both events, the P- and S-waves will intersect the FOC with distinct incidence angles, which subsequently impacts the amplitude of the analyzed velocity component.
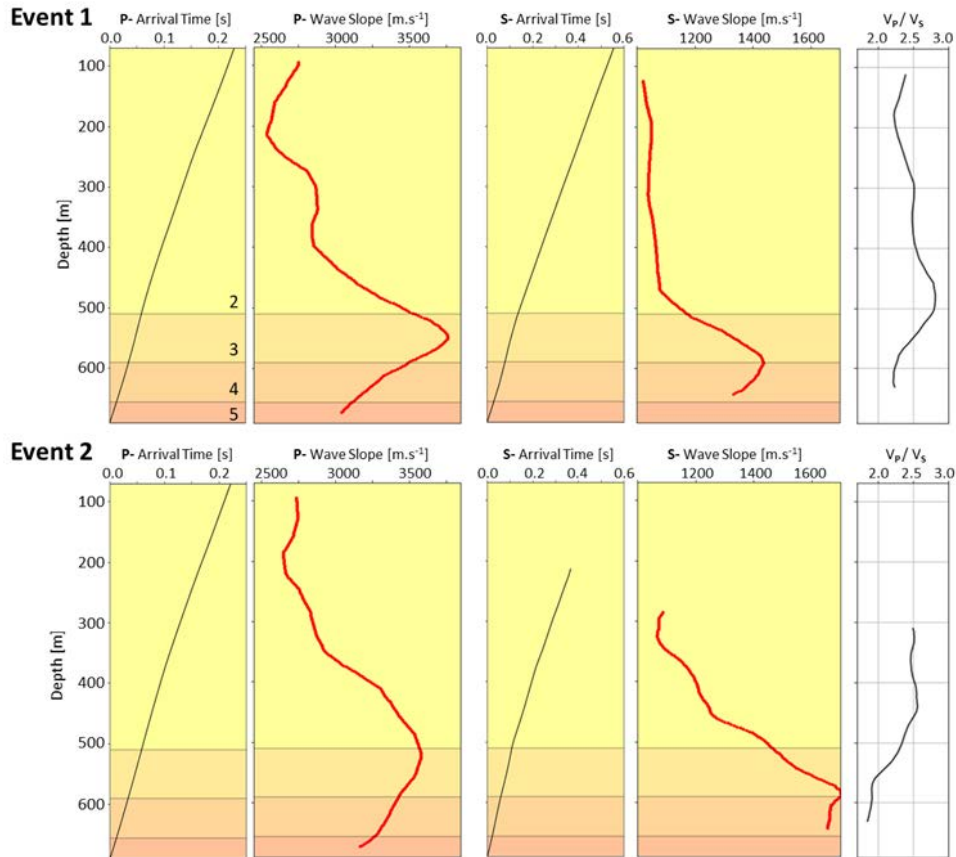
Figure 6: P- and S-wave arrival times (left panels, black curve) and slopes (right panels, red curve) for the February (Event 1, top) and the April (Event 2, bottom) events. A moving average filter whose period corresponds to the local wavelength is applied on the raw slope profile before plotting. The background colour shows the lithological changes and the numbers of the top-left panel refer to the column presented in Fig. 1c). For each event, the right hand side panel shows the VP/VS ratios computed from the slope profiles.

For both events, VP/VS ratio profiles have been computed from the derived velocities. The computed ratios show local variations within the investigated depths and a decrease of the ratio is observed for both events around 500 m. The absolute values and the location of the apparent decrease in VP/VS are consistent with the Wadati diagram computed from the February record. In addition, the strong variations observed below 700 m (TVD) and the VP/VS ratio measurements are consistent with analogue analysis at the study site (e.g. Wawerzinek et al. (2021)).

5. **Discussion**

At the light of the results of the 6-month continuous monitoring period, we now evaluate the usability of DAS in the routine operation of the geothermal plant.

5.1. Logging and monitoring capabilities of DAS along well

While the logging capabilities of DTS and DSS have been applied since decades (Förster et al., 1997; Hurtig et al., 1994), previous studies have shown that DAS can also provide insight into the well and surrounding structures, in particular when focussing on their lower frequency content. For example, Bruno et al. (2018) reported on the effectiveness of DAS technology for measuring the hydromechanical response caused by fractures in a reservoir. At the Reykjanes geothermal field (Iceland), Raab et al. (2019) show that variations and patterns in a cement bond log (CBL) are correlated with the average strain-rate DAS data acquired behind casing and under noisy well drilling and testing conditions. CBL are generally used to check the casing cementation job, which constitutes one aspect of the well integrity assessment. Correlation of DAS background noise and CBL indicates the possibility to monitor - continuously - the well cementation from DAS data. This aspect is investigated as in well TH3 (Fig. 4b and 4c). Hence, the evolution with depth of the average DAS spectral energy below 0.1 Hz, or between 5 and 40 Hz (black curve), is plotted next to the CBL acquired in TH3 in December 2019 (red curve). Usually, amplitudes of CBL are smaller with a good cement bond than with a partial bond, or no bond at all (free pipe). Out of the shallowest part above 50 m where surface noise has a significant impact on the presented energy profile (see dotted part of the black curve), the DAS and CBL curves present similarities, especially around 200 and 600 m. At these depths, both profiles show very similar variations, which suggest that a poorer cement bond and fiber coupling may explain the higher noise level observed in the strain-rate data. However, a perfect match between the profiles cannot be demonstrated along the entire fiber. In particular, the high energies observed locally at 350 and 400 m, disturbing the spectra over the whole frequency range (Fig. 4a), cannot be associated with a peculiar cementation zone, according to the CBL. On the other hand, the present CBL delivers a directional but unoriented measure of the cement bond and does not allow the analysis of potential azimuthal variations of the cement quality nor channelling effects. The mechanical coupling of the fiber could therefore be locally weaker without noticeable evidence on the CBL. The plant operation may also contribute to the observation of local disturbances. The various datasets presented in the time domain (Fig. 3 and 5) show short depth intervals of higher strain-rate. The changing location of the noisy intervals over time suggests that the underlying source is not static and cannot be attributed to the well structure.

Besides the logging capabilities of the DAS, the detection of the two local microseismic events presented in Sect. 4 also supports the relevance of monitoring using DAS along wells. In addition, the intrinsic linear array-type nature of DAS provides advantageous insight into the seismic source. Hence, DAS advantageously complements standard monitoring approaches of geothermal fields from surface (e.g. Baisch et al. (2014)):

- For both events, multiple P- and S-phases could be identified along the vertical section of the well, which proves the capacity of DAS to consolidate the records delivered by three-component seismometers and opens promising perspectives in terms of localization and characterization of the event. Lior et al. (2021) showed in particular the ability of DAS-based approaches to resolve source parameters using P-waves on horizontal ocean-bottom fibers. The utilization of the DAS waveforms for the further characterization of the seismic source is currently investigated.

© BY

- In addition, the level of detection achieved for the April event demonstrates the capability of the technology to monitor a geothermal field in an urban area. The FOC cemented behind the well casing acts effectively as a long string of sensors deployed closer to the monitoring target, which eventually detect weak events whose low magnitude prevents surface seismometers from identifying them.

- For the April event, the characteristic functions of the recursive STA/LTA (Fig. 7) show concomitant P- and S-waves triggers and give evidence of satisfactory signal-to-noise ratios, despite the apparent low magnitude of the event (Sect. 4.2.1). Figure 7b) shows in particular that the STA/LTA ratio exceeds three for the S-waves in the deepest levels. The figure highlights as well that fewer and sparser traces are triggered between surface and 200 m, which was previously identified as an interval strongly perturbed by anthropogenic noise (see Sect. 4.1).
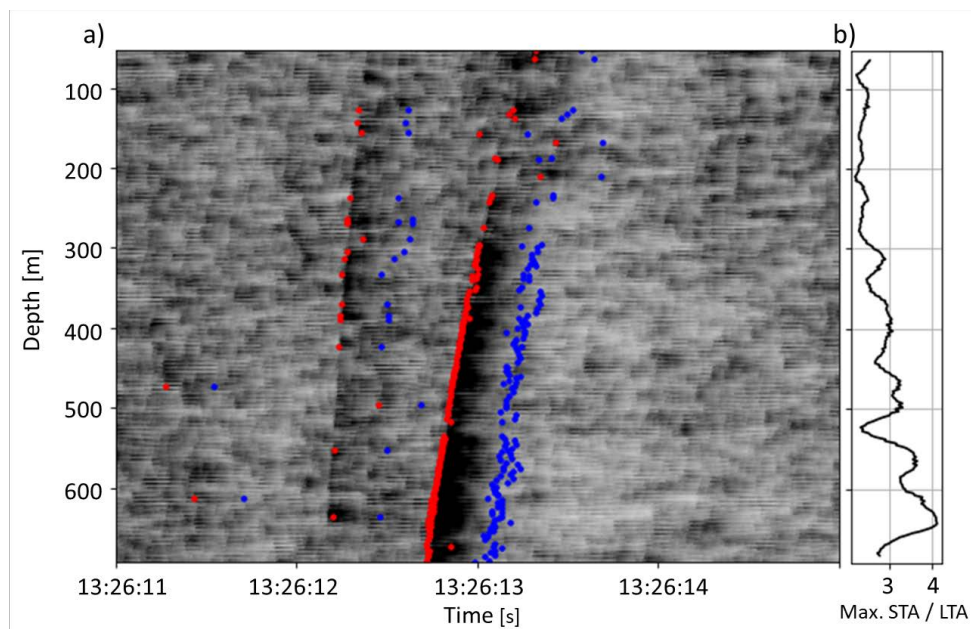
Figure 7: Characterization of the level of sensitivity in the detection of the April event. Panel a): characteristic functions of the recursive STA/LTA algorithm which has been applied to each strain-rate time-series. Red and blue dots show respectively the coordinates at which the trigger turns on and off, provided the parameters shown in Table 1. Panel b): evolution with depth of the maximum STA/LTA ratio measured along the characteristic functions presented in panel a).

To some extent, the aforementioned monitoring and logging capabilities can be compared to those of a string of geophones. However, DAS prevents from locating an event using one single monitoring well because of the broadside insensitivity of the current fiber set-up. Although offset and depth of the event could be determined, the back azimuth would remain unknown. This limitation could be minimized for FOC deployed along deviated wells. Besides, technological solutions are currently investigated to overcome the broadside insensitivity of DAS, using in particular helically wound fibers (Hornman, 2017). Hence, unless several sites or wells would be instrumented with FOCs for DAS, the latter needs to be complemented by other equipment (e.g. surface seismometers) to be able to reach seismic monitoring objectives (e.g. location capabilities), but possibly at the cost of a higher magnitude

616 of completeness. Nevertheless, the previously mentioned logging capabilities of DAS are enhanced by
617 the high spatial sampling achievable along large distances. Furthermore, these logging capacities are
618 enriched by the possibility delivered by one single sensing element to monitor various physical
619 parameters. Indeed, a FOC is usually made of several single and multi-mode fibers that can be used
620 for a variety of applications. This potential has been evidenced and leveraged by the oil and gas
621 industry for around one decade (Koelman et al., 2012; Koelman, 2011; Van Der Horst et al., 2013).

5.2. Towards real-time seismic monitoring of geothermal plants

623 The use of DAS for monitoring geothermal plant operations requires a degree of sensitivity in detecting
624 events, which has been demonstrated in Sect. V.1. For mitigation purposes, the monitoring system
625 must also provide the results, i.e. seismic activity catalogues, as fast as possible. The implementation
626 of a DAS system into the monitoring strategy of the geothermal plant calls therefore for efficient
627 transfer of large amounts of data in addition to fast and secured data access for optimized processing.
628 These needs were met with the Azure cloud platform, which offered a unified service that combined
629 storage, accessibility and data processing. During the 6-months monitoring period, processing of 1-
630 minute long DAS acquisitions, besides the 1-hour long datasets, was also carried out to move towards
631 real-time processing. During the dataset formatting, each file was concatenated with 10 seconds of
632 the preceding one to avoid missing events at the edge of the datasets (due to filter initiation). The
633 processing of each file, according to the workflow described in Section III, took on average between 9
634 and 10 s, which is significantly less than the file duration and thus avoids the occurrence of overflows.
635 To tend towards real-time processing of the acquired datasets, two limiting factors are identified:

636   -   the buffering of the files on the recorder. In its current operating condition, the system needs
637   an HDF5 file to be fully written to the A1-R recorder's buffer to be pushed towards the Data
638   Lake. Such a technical limitation could be overcome by adapting the recorder's software with
639   the goal of streaming the data towards the IoT cloud platform on a real-time basis.
640   -   the file transfer through the wired connection. The band-pass of the wired connection being
641   limited, this necessarily adds a lag time in the data processing. For short files, this limitation is
642   much less restrictive than the files buffering: with the observed uploading rate of 36 MB/s,
643   less than three seconds are theoretically necessary to upload one-minute-long files on the
644   Data Lake.

645 In practice, these two factors delayed the data processing by about 10 more seconds. Hence, the
646 processing flow allowed to deliver automatic detection results with a maximal delay of approximately
647 1 min 20 s after the event onset time, which shows great potential for real-time monitoring.

5.3. Outlook for a Reservoir Management System

649 In order to minimize risks and optimize operational parameters, the real-time integration of
650 monitoring outcomes and associated forecasts into the exploitation of geothermal sites is a critical
651 aspect for the geothermal operators. At the SLS geothermal plant, work on this issue has recently led
652 to the development of a concept of what would constitute a reservoir management system (RMS)
653 (Gaucher et al., 2022). By merging observations and forecasts, the system should be able to propose
654 the geothermal field operator alternative production scenarios to mitigate immediate or forecasted
655 risks.

656 The system is composed of three main modules, which are linked and interact with each other
657 (Gaucher et al., 2022). A database is designed to store the monitoring observations acquired in the
658 field, the results of their processing and the risk projections. The database is in interaction with the

659 processing centre, which is necessary to update the results of the observations and numerical
660 modelling. Finally, the dashboard synthesizes all available information with a finite number of key
661 indicators and interfaces with the operators. The latter aims to facilitate decision making based on the
662 observations and modelled predictions.

663 The monitoring system tested at the SLS geothermal site during the 6-months period demonstrates,
664 with respect to the described RMS, the technical feasibility of acquiring, processing and archiving large
665 amounts of passive seismic data, as encountered with DAS. The supporting IoT platform routinely used
666 by the field operator proved to be a viable solution, which moreover features scalable processing and
667 archiving resources in addition to user-dependent access authorizations to guarantee data
668 confidentiality. Hence, the DAS monitoring system could be seen as a prototype linking the monitoring
669 outcomes to the central database and using some of the features of the processing centre, while
670 operating in a real operational environment.

671 Conclusion

672 In this work, we describe the monitoring concept that has been developed to establish DAS as an
673 effective component of the seismic monitoring of the Schäftlarnstraße geothermal plant, located in
674 the inner city of Munich. The described monitoring system links the on-site infrastructure, which
675 includes the interrogated fiber and the DAS recorder, to a cloud IoT platform designed to deliver both
676 a secured storage environment for the DAS acquisitions, and optimized IT resources for their
677 processing. The 6-months testing period and the related outcomes can be seen as a proof of concept,
678 showing the viability of the proposed monitoring system and, thereby, the feasibility of acquiring
679 continuous DAS data in geothermal wells under operational conditions, while efficiently managing and
680 processing the large and continuous flow of DAS records.

681 The technical characteristics of the cloud platform supporting the monitoring concept, which features
682 scalable and performant storage and processing resources, open interesting perspectives for the
683 densely sampled DAS acquisitions to be used in quasi-real time assessment of induced seismicity. For
684 mitigation purposes, we demonstrate the usability of the proposed concept to report on seismic event
685 detections with low latency while processing minute-long data blocks.

686 The integration of DAS into the monitoring operations requires additionally a degree of sensitivity in
687 detecting events. The relevance of using DAS in the seismic monitoring operations is demonstrated by
688 the observations collected during the 6-months testing period. In particular, the level of detection
689 achieved for a low magnitude event occurring near the geothermal boreholes demonstrates the
690 capability of the technology to monitor a geothermal field under high anthropogenic noise conditions.
691 The quality of the DAS data is evidenced by the high spatial coherence observed for both P- and S-
692 waves over the entire FOC, as well as the measured signal-to-noise ratio, especially for S-waves. The
693 demonstrated level of sensitivity results mainly from the proximity of the borehole DAS sensors to the
694 assumed location of induced seismicity, and from the application of advanced detection (network
695 coincidence) and denoising (*f-k* filtering) techniques that take advantage of the high spatial and
696 temporal sampling of the acquisitions. Hence, DAS advantageously complements standard monitoring
697 approaches based on surface deployments, allowing the detection of events that individual
698 seismometers may fail to record.

699 Our study also highlights the possible dual use of DAS from the detailed analysis of two local seismic
700 events, using in particular the measured onset-time of P- and S-waves. On one hand, DAS allows dense
701 sampling of the P- and S-waves arrival times along the fiber. This set of observations supports the
702 further evaluation and analysis of spatial variations of P- and S-waves apparent velocities along the
703 fiber. The variations in apparent velocities and apparent VP/VS ratios presented for the two local

704   seismic events highlight local structural changes in the medium surrounding the TH3 fiber. Beside site
705   characterization, the arrival times contribute to the preliminary characterization of the seismic event
706   using Wadati diagrams, giving access to the time, depth and offset of the seismic event origin. On the
707   other hand, the broadside insensitivity of the applied DAS technology can restrict its capabilities for
708   extensive seismic source characterization. The monitoring based on one single vertical DAS antenna
709   cannot be considered as a stand-alone solution to meet the requirements associated with the seismic
710   monitoring of the SLS site, as complementary viewpoints would be necessary for a precise evaluation,
711   in particular, of the seismic source back-azimuth.

712   However, the present study demonstrates that the deployment of FOC in geothermal wells opens
713   perspectives that extend beyond seismic monitoring. Benefiting from the broadband sensitivity and
714   high spatial sampling of DAS, we show a correlation between the CBL and the spatial evolution of the
715   spectral energy of DAS strain-rate. The measurement suggests that higher noise-levels observed in the
716   DAS data may be associated with a weaker mechanical coupling of the fiber and a weaker cement
717   bond, leading to interesting prospects for the continuous well surveillance. More generally, DOFS
718   provide a cost-effective sensing element to implement logging, imaging and monitoring capabilities
719   all over the lifetime of a borehole, in an operational environment (e.g. Li et al. (2015)). The interest of
720   the geothermal energy industry in DOFS lies therefore in the potential of a single sensing element to
721   provide information on temperature profiles, in- and out-flow zones of the geothermal fluid along the
722   well (Schölderle et al., 2021), well integrity (cement bond log, leakage through casing) and, as
723   discussed, advantageous seismic monitoring perspective.

724

Appendix

Appendix A
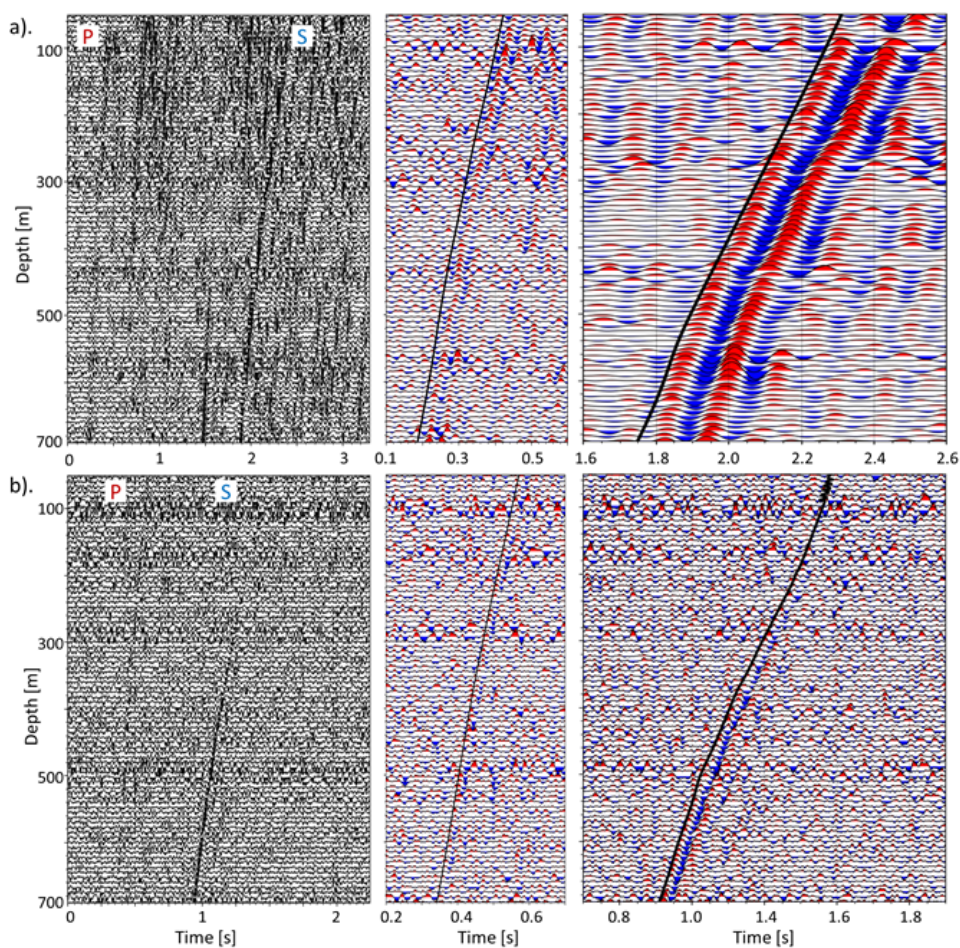
Figure A1: Same as Fig. 5, without denoising the strain-rate datasets in the f-k domain. Here, we only apply a bandpass filter between 5 and 40 Hz to the data. In comparison with Fig. 5, this figure highlights the effect of the f-k filtering on the spatial coherence of the upwards-traveling wavefronts.

733   Appendix B
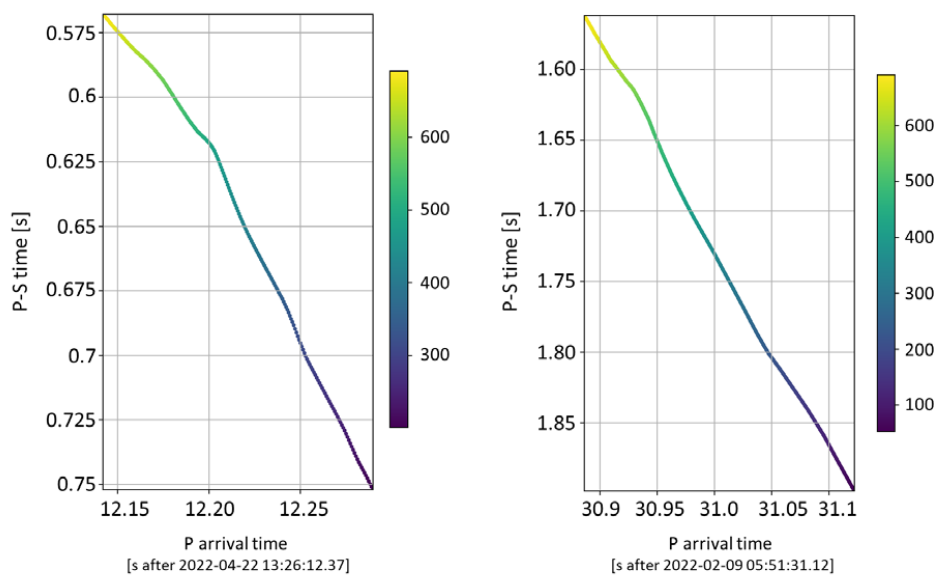
734

735   *Figure B1: Wadati diagrams computed using the P- and S-wave arrival times associated with the*
736   *February (left) and the April (right) events. The colormap shows the depth (TVD) of the virtual DAS*
737   *sensors along the TH3 fiber.*
738

Author contributions

JA designed the algorithms, performed the analysis and wrote the initial draft.

EG contributed to the discussion and extensively reviewed the article.

KT coordinated, for the geothermal operator (SWM GmbH), the 6-month monitoring test and reviewed the article.

Competing interests

The authors declare no competing interests.

Acknowledgments

This work was conducted in the frame of the INSIDE project (https://inside-geothermie.de/en/inside-en/), which is supported by the German Federal Ministry for Economic Affairs and Climate Action and the Project Management Jülich (PtJ) under the grant agreement number 03EE4008C. We would like to express particular thanks to the IT-department of Stadtwerke München (SWM GmbH), and more particularly to Georg Aures, Maximilian Hansinger and Bettina Hille, for their support in setting up the accesses on the Azure account and managing the DAS data flow within the company's intranet. We also thank FEBUS Optics for their logistical support and the adjustment of the hardware of the A1-R recorder to suit the needs expressed by this study. Finally, we would like to thank all the partners of the INSIDE project, Innovative Energie für Pullach GmbH (IEP GmbH), Erdwerk GmbH and Stadtwerke München (SWM GmbH), for their fruitful contribution to the INSIDE project.

Data and code availability

The DAS strain rate datasets corresponding to the two events studied in the paper and the scripts used on the computing instances for loading and processing the DAS datasets are made available to the reviewers using the KIT file sharing system at following URL: https://bwsyncandshare.kit.edu/s/rsXtdf6Z9Af27L9. The data and code are in process of being made public from the KIT Open Access repository (https://www.bibliothek.kit.edu/kitopen.php).

Abbreviations

DAS: Distributed acoustic sensing

DOFS: Distributed optical fiber sensors

DSS: Distributed strain sensing

DTS: Distributed temperature sensing

ESP: Electric submersible pumps

f-k: Frequency-wavenumber

FOC: Fiber optic cable

771   HDF5: Hierarchical Data Format version 5

772   IaaS: Infrastructure as a service

773   IoT: Internet of things

774   LTA: Long time average

775   OTDR: Optical time domain reflectometry

776   OMM: Obere Meeresmolasse

777   OSM: Obere Süßwasser Molass

778   PaaS: Platform as a service

779   RAM: Random access memory

780   SAS: Shared access signature

781   SBM: Süßbrackwassermolasse

782   SLS: Schäftlarnstraße

783   SR: Strain-rate

784   SSD: Solid-state drive

785   STA: Short time average

786   TVD: True vertical depth

787

References

Agemar, T., Schellschmidt, R., and Schulz, R.: Subsurface temperature distribution in Germany, Geothermics, 44, 65–77, https://doi.org/10.1016/j.geothermics.2012.07.002, 2012.

Agemar, T., Weber, J., and Schulz, R.: Deep Geothermal Energy Production in Germany, Energies, 7, 4397–4416, https://doi.org/10.3390/en7074397, 2014.

Ajo-Franklin, J. B., Dou, S., Lindsey, N. J., Monga, I., Tracy, C., Robertson, M., Rodriguez Tribaldos, V., Ulrich, C., Freifeld, B., Daley, T., and Li, X.: Distributed Acoustic Sensing Using Dark Fiber for Near-Surface Characterization and Broadband Seismic Event Detection, Sci Rep, 9, 1328, https://doi.org/10.1038/s41598-018-36675-8, 2019.

Azzola, J., Gaucher, E., Bögelspacher, F., Ralph, B., Betz, B., and Ilka, S.: INSIDE: Investigating the impact of geothermal exploitation in the Munich area: the induced seismicity perspective. Presented at the European Geothermal Workshop (EGW), Karlsruhe, Germany, 2021.

Azzola, J., Gaucher, E., Ralph, B., and Ilka, S.: Deployment of a Distributed Fiber Optic Sensing (DFOS) monitoring station in Munich within INSIDE project. Presented at the 82nd annual meeting of the Deutschen Physikalischen Gesellschaft (DGG 2022), Online, 2022.

Baldwin, C. S.: Brief history of fiber optic sensing in the oil field industry, SPIE Sensing Technology + Applications, Baltimore, Maryland, USA, 909803, https://doi.org/10.1117/12.2050550, 2014.

Beyreuther, M., Barsch, R., Krischer, L., Megies, T., Behr, Y., and Wassermann, J.: ObsPy: A Python Toolbox for Seismology, Seismological Research Letters, 81, 530–533, https://doi.org/10.1785/gssrl.81.3.530, 2010.

Boer, J. J. den, Mateeva, A. A., Pearce, J. G., Mestayer, J. J., Birch, W., Lopez, J. L., Hornman, J. C., and Kuvshinov, B. N.: Detecting broadside acoustic signals with a fiber optical distributed acoustic sensing (DAS) assembly, 2017.

Böhm, F., Savvatis, A., Steiner, U., Schneider, M., and Koch, R.: Lithofazielle Reservoircharakterisierung zur geothermischen Nutzung des Malm im Großraum München, Grundwasser, 18, 3–13, https://doi.org/10.1007/s00767-012-0202-4, 2013.

Bruno, M. S., Lao, K., Oliver, N., Becker, M., and California State University, Long BeachSilixa LLC: Use of Fiber Optic Distributed Acoustic Sensing for Measuring Hydraulic Connectivity for Geothermal Applications, https://doi.org/10.2172/1434494, 2018.

Correa, J., Egorov, A., Tertyshnikov, K., Bona, A., Pevzner, R., Dean, T., Freifeld, B., and Marshall, S.: Analysis of signal to noise and directivity characteristics of DAS VSP at near and far offsets — A CO2CRC Otway Project data example, The Leading Edge, https://doi.org/10.1190/tle36120994a1.1, 2017.

Cröniger, C., Tretter, R., Eichenseer, P., Kleinertz, B., Timpe, C., Bürger, V., and Cludius, J.: Approach to Climate Neutral Heat Supply in Munich 2035. Presented at the European Geothermal Congress (EGC), Berlin, Germany, 2022.

Duncan, G. and Beresford, G.: Slowness adaptive f-k filtering of prestack seismic data, GEOPHYSICS, 59, 140–147, https://doi.org/10.1190/1.1443525, 1994.

Dussel, M., Lüschen, E., Thomas, R., Agemar, T., Fritzer, T., Sieblitz, S., Huber, B., Birner, J., and Schulz, R.: Forecast for thermal water use from Upper Jurassic carbonates in the Munich region (South German Molasse Basin), Geothermics, 60, 13–30, https://doi.org/10.1016/j.geothermics.2015.10.010, 2016.

Farquharson, N., Schubert, D. A., and Steiner, U.: Geothermal Energy in Munich (and Beyond) A Geothermal City Case Study, 8, 2016.

Gaucher, E., Schoenball, M., Heidbach, O., Zang, A., Fokker, P. A., van Wees, J.-D., and Kohl, T.: Induced seismicity in geothermal reservoirs: A review of forecasting approaches, Renewable and Sustainable Energy Reviews, 52, 1473–1490, https://doi.org/10.1016/j.rser.2015.08.026, 2015.

Gaucher, E., Hansinger, M., Goblirsch, P., Azzola, J., and Thiemann, K.: Towards a geothermal reservoir management system. Presented at the European Geothermal Congress (EGC), Berlin, Germany, 2022.

838   Grigoli, F., Cesca, S., Priolo, E., Rinaldi, A. P., Clinton, J. F., Stabile, T. A., Dost, B., Fernandez, M. G.,
839   Wiemer, S., and Dahm, T.: Current challenges in monitoring, discrimination, and management
840   of induced seismicity related to underground industrial activities: A European perspective:
841   CHALLENGES IN INDUCED SEISMICITY, Reviews of Geophysics, 55, 310–340,
842   https://doi.org/10.1002/2016RG000542, 2017.
843   Harris, K., White, D., Melanson, D., Samson, C., and Daley, T. M.: Feasibility of time-lapse VSP
844   monitoring at the Aquistore CO2 storage site using a distributed acoustic sensing system,
845   International Journal of Greenhouse Gas Control, 50, 248–260,
846   https://doi.org/10.1016/j.ijggc.2016.04.016, 2016.
847   Hartog, A., Kotov, O. I., and Liokumovich, L. B.: The Optics of Distributed Vibration Sensing, Second
848   EAGE Workshop on Permanent Reservoir Monitoring 2013 – Current and Future Trends,
849   Stavanger, Norway, https://doi.org/10.3997/2214-4609.20131301, 2013.
850   Hartog, A. H.: An Introduction to Distributed Optical Fibre Sensors, 1st ed., CRC Press,
851   https://doi.org/10.1201/9781315119014, 2017.
852   Hornman, J. C.: Field trial of seismic recording using distributed acoustic sensing with broadside
853   sensitive fibre-optic cables: Field trial of seismic recording, Geophysical Prospecting, 65, 35–46,
854   https://doi.org/10.1111/1365-2478.12358, 2017.
855   Isken, M. P., Vasyura-Bathke, H., Dahm, T., and Heimann, S.: De-noising distributed acoustic sensing
856   data using an adaptive frequency–wavenumber filter, Geophysical Journal International, 231,
857   944–949, https://doi.org/10.1093/gji/ggac229, 2022.
858   Johannessen, K., Drakeley, B., and Farhadiroushan, M.: Distributed Acoustic Sensing - A New Way of
859   Listening to Your Well/Reservoir, in: All Days, SPE Intelligent Energy International, Utrecht, The
860   Netherlands, SPE-149602-MS, https://doi.org/10.2118/149602-MS, 2012.
861   Juškaitis, R., Mamedov, A. M., Potapov, V. T., and Shatalin, S. V.: Interferometry with Rayleigh
862   backscattering in a single-mode optical fiber, Opt. Lett., 19, 225,
863   https://doi.org/10.1364/OL.19.000225, 1994.
864   Koelman, J. M., Lopez, J. L., and Potters, J. H.: Optical Fibers: The Neurons For Future Intelligent Wells,
865   in: All Days, SPE Intelligent Energy International, Utrecht, The Netherlands, SPE-150203-MS,
866   https://doi.org/10.2118/150203-MS, 2012.
867   Koelman, J. V.: Fiber-Optic Sensing Technology Providing Well, Reservoir Information - Anyplace,
868   Anytime, Journal of Petroleum Technology, 63, 22–24, https://doi.org/10.2118/0711-0022-JPT,
869   2011.
870   Kraft, T., Mai, P. M., Wiemer, S., Deichmann, N., Ripperger, J., Kästli, P., Bachmann, C., Fäh, D.,
871   Wössner, J., and Giardini, D.: Enhanced Geothermal Systems: Mitigating Risk in Urban Areas,
872   Eos, Transactions American Geophysical Union, 90, 273–274,
873   https://doi.org/10.1029/2009EO320001, 2009.
874   Lellouch, A., Lindsey, N. J., Ellsworth, W. L., and Biondi, B. L.: Comparison between Distributed Acoustic
875   Sensing and Geophones: Downhole Microseismic Monitoring of the FORGE Geothermal
876   Experiment, Seismological Research Letters, 91, 3256–3268,
877   https://doi.org/10.1785/0220200149, 2020.
878   Li, M., Wang, H., and Tao, G.: Current and Future Applications of Distributed Acoustic Sensing as a New
879   Reservoir Geophysics Tool, TOPEJ, 8, https://doi.org/10.2174/1874834120150625E008, 2015.
880   Lindsey, N. J., Rademacher, H., and Ajo-Franklin, J. B.: On the Broadband Instrument Response of Fiber-
881   Optic DAS Arrays, J. Geophys. Res. Solid Earth, 125, https://doi.org/10.1029/2019JB018145,
882   2020.
883   Lior, I., Sladen, A., Mercerat, D., Ampuero, J.-P., Rivet, D., and Sambolian, S.: Strain to ground motion
884   conversion of distributed acoustic sensing data for earthquake magnitude and stress drop
885   determination, Solid Earth, 12, 1421–1442, https://doi.org/10.5194/se-12-1421-2021, 2021.
886   Madsen, K., Parker, T., and Gaston, G.: A VSP Field Trial Using Distributed Acoustic Sensing in a
887   Producing Well in the North Sea, 74th EAGE Conference and Exhibition incorporating EUROPEC
888   2012, Copenhagen, Denmark, https://doi.org/10.3997/2214-4609.20148801, 2012.

889   Masoudi, A., Newson, T.P.: Contributed Review: Distributed optical fibre dynamic strain sensing.
890   Review of Scientific Instruments 87, 011501. https://doi.org/10.1063/1.4939482, 2016
891   Mateeva, A., Mestayer, J., Cox, B., Kiyashchenko, D., Wills, P., Lopez, J., Grandi, S., Hornman, K.,
892   Lumens, P., Franzen, A., Hill, D., and Roy, J.: Advances in Distributed Acoustic Sensing (DAS) for
893   VSP, in: SEG Technical Program Expanded Abstracts 2012, SEG Technical Program Expanded
894   Abstracts 2012, 1–5, https://doi.org/10.1190/segam2012-0739.1, 2012.
895   Mateeva, A., Lopez, J., Potters, H., Mestayer, J., Cox, B., Kiyashchenko, D., Wills, P., Grandi, S.,
896   Hornman, K., Kuvshinov, B., Berlang, W., Yang, Z., and Detomo, R.: Distributed acoustic sensing
897   for reservoir monitoring with vertical seismic profiling: Distributed acoustic sensing (DAS) for
898   reservoir   monitoring   with   VSP,   Geophysical   Prospecting,   62,   679–692,
899   https://doi.org/10.1111/1365-2478.12116, 2014.
900   McNamara, D. E.: Ambient Noise Levels in the Continental United States, Bulletin of the Seismological
901   Society of America, 94, 1517–1527, https://doi.org/10.1785/012003001, 2004.
902   Megies, T. and Wassermann, J.: Microseismicity observed at a non-pressure-stimulated geothermal
903   power plant, Geothermics, 52, 36–49, https://doi.org/10.1016/j.geothermics.2014.01.002,
904   2014.
905   Miller, D. E., Daley, T. M., White, D., Freifeld, B. M., Robertson, M., Cocker, J., and Craven, M.:
906   Simultaneous Acquisition of Distributed Acoustic Sensing VSP with Multi-mode and Single-mode
907   Fiber-optic Cables and 3C-Geophones at the Aquistore CO2 Storage Site, 14, 2016.
908   Naldrett, G., Cerrahoglu, C., and Mahue, V.: Production Monitoring Using Next-Generation Distributed
909   Sensing Systems, Petro S Journ, 59, 496–510, https://doi.org/10.30632/PJV59V4-2018a5, 2018.
910   Olofsson, B. and Martinez, A.: Validation of DAS data integrity against standard geophones — DAS
911   field   test   at   Aquistore   site,   The   Leading   Edge,   36,   981–986,
912   https://doi.org/10.1190/tle36120981.1, 2017.
913   Paitz, P., Edme, P., Gräff, D., Walter, F., Doetsch, J., Chalari, A., Schmelzbach, C., and Fichtner, A.:
914   Empirical Investigations of the Instrument Response for Distributed Acoustic Sensing (DAS)
915   across   17   Octaves,   Bulletin   of   the   Seismological   Society   of   America,   111,   1–10,
916   https://doi.org/10.1785/0120200185, 2021.
917   Parker, T., Shatalin, S., and Farhadiroushan, M.: Distributed Acoustic Sensing – a new tool for seismic
918   applications, 32, 9, 2014.
919   Raab, T. ., Reinsch, T. ., Aldaz Cifuentes, S. R., and Henninges, J. .: Real-Time Well-Integrity Monitoring
920   Using   Fiber-Optic   Distributed   Acoustic   Sensing,   SPE   Journal,   24,   1997–2009,
921   https://doi.org/10.2118/195678-PA, 2019.
922   Reinsch, T., Henninges, J., and Ásmundsson, R.: Thermal, mechanical and chemical influences on the
923   performance of optical fibres for distributed temperature sensing in a hot geothermal well,
924   Environ Earth Sci, 70, 3465–3480, https://doi.org/10.1007/s12665-013-2248-8, 2013.
925   Schölderle, F., Lipus, M., Pfrang, D., Reinsch, T., Haberer, S., Einsiedl, F., and Zosseder, K.: Monitoring
926   cold water injections for reservoir characterization using a permanent fiber optic installation in
927   a geothermal production well in the Southern German Molasse Basin, Geotherm Energy, 9, 21,
928   https://doi.org/10.1186/s40517-021-00204-0, 2021.
929   Schulz, R. and Jobmann, M.: Hydrogeothermische Energiebilanz und Grundwasserhaushalt des
930   Malmkarstes im Süddeutschen Molassebecken, Teilgebiet: Hydrogeothermik; Final Report,
931   Institut für Geowissenschaftliche Gemeinschaftsaufgaben (GGA): Hannover, Germany, Archive
932   Number 105040, 1989.
933   Seithel, R., Gaucher, E., Mueller, B., Steiner, U., and Kohl, T.: Probability of fault reactivation in the
934   Bavarian   Molasse   Basin,   Geothermics,   82,   81–90,
935   https://doi.org/10.1016/j.geothermics.2019.06.004, 2019.
936   Soh, J., Copeland, M., Puca, A., and Harris, M.: Overview of Azure Infrastructure as a Service (IaaS)
937   Services, in: Microsoft Azure: Planning, Deploying, and Managing the Cloud, edited by: Soh, J.,
938   Copeland,   M.,   Puca,   A.,   and   Harris,   M.,   Apress,   Berkeley,   CA,   21–41,
939   https://doi.org/10.1007/978-1-4842-5958-0_2, 2020a.

940 Soh, J., Copeland, M., Puca, A., and Harris, M.: Overview of Azure Platform as a Service, in: Microsoft
941   Azure: Planning, Deploying, and Managing the Cloud, edited by: Soh, J., Copeland, M., Puca, A.,
942   and Harris, M., Apress, Berkeley, CA, 43–55, https://doi.org/10.1007/978-1-4842-5958-0_3,
943   2020b.
944 Trnkoczy, A.: Understanding and parameter setting of STA/LTA trigger algorithm, pp. 1-20 pp., 2012.
945 Van Der Horst, J., Lopez, J. L., Berlang, W., and Potters, H.: In-Well Distributed Fiber Optic Solutions
946   for Reservoir Surveillance, in: All Days, Offshore Technology Conference, Houston, Texas, USA,
947   OTC-23949-MS, https://doi.org/10.4043/23949-MS, 2013.
948 Wadati, K. and Oki, S.: On the Travel Time of Earthquake Waves. (Part II), Journal of the Meteorological
949   Society of Japan, 11, 14–28, https://doi.org/10.2151/jmsj1923.11.1_14, 1933.
950 Wawerzinek, B., Buness, H., von Hartmann, H., and Tanner, D. C.: S-wave experiments for the
951   exploration of a deep geothermal carbonate reservoir in the German Molasse Basin, Geotherm
952   Energy, 9, 6, https://doi.org/10.1186/s40517-021-00189-w, 2021.
953 Withers, M., Aster, R., Young, C., Beiriger, J., Harris, M., Moore, S., and Trujillo, J.: A comparison of
954   select trigger algorithms for automated global seismic phase and event detection, Bulletin of
955   the Seismological Society of America, 88, 95–106, https://doi.org/10.1785/BSSA0880010095,
956   1998.

957 Zhirnov, A. A., Stepanov, K. V., Chernutsky, A. O., Fedorov, A. K., Nesterov, E. T., Svelto, C., Pnev, A. B.,
958   and Karasik, V. E.: Influence of the Laser Frequency Drift in Phase-Sensitive Optical Time Domain
959   Reflectometry, Opt. Spectrosc., 127, 656–663, https://doi.org/10.1134/S0030400X1910031X,
960   2019.